Supporting Information

Collaborative Mechanistic Effects between Vanadia and Titania during the Oxidative Dehydrogenation of Propane Investigated by Operando and Transient Spectroscopy

Leon Schumacher, Johannes Pfeiffer, Jun Shen, Torsten Gutmann, Hergen Breitzke, Gerd Buntkowsky, Kathrin Hofmann, Christian Hess*

Technical University of Darmstadt, Department of Chemistry, Eduard-Zintl-Institut für Anorganische und Physikalische Chemie, Alarich-Weiss-Str. 8, 64287 Darmstadt, Germany

*Corresponding Author (E-Mail: christian.hess@tu-darmstadt.de)

Table of Contents:

1) Technical Information

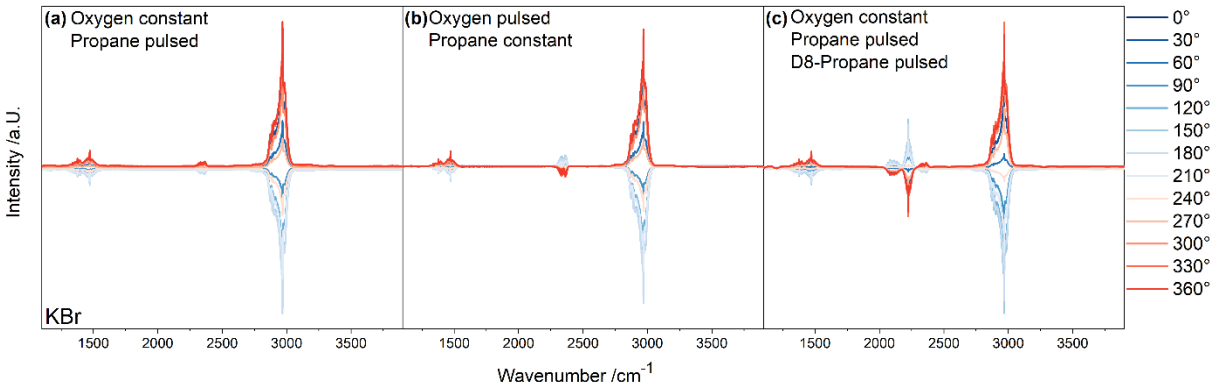

Figure S1: PSD spectra of KBr during **(a)** constant oxygen and pulsed propane, **(b)** pulsed oxygen and constant propane, and **(c)** constant oxygen and pulsed h8-propane/d8-propane as a background for the sample PSD spectra in a 30° phase angle resolution.

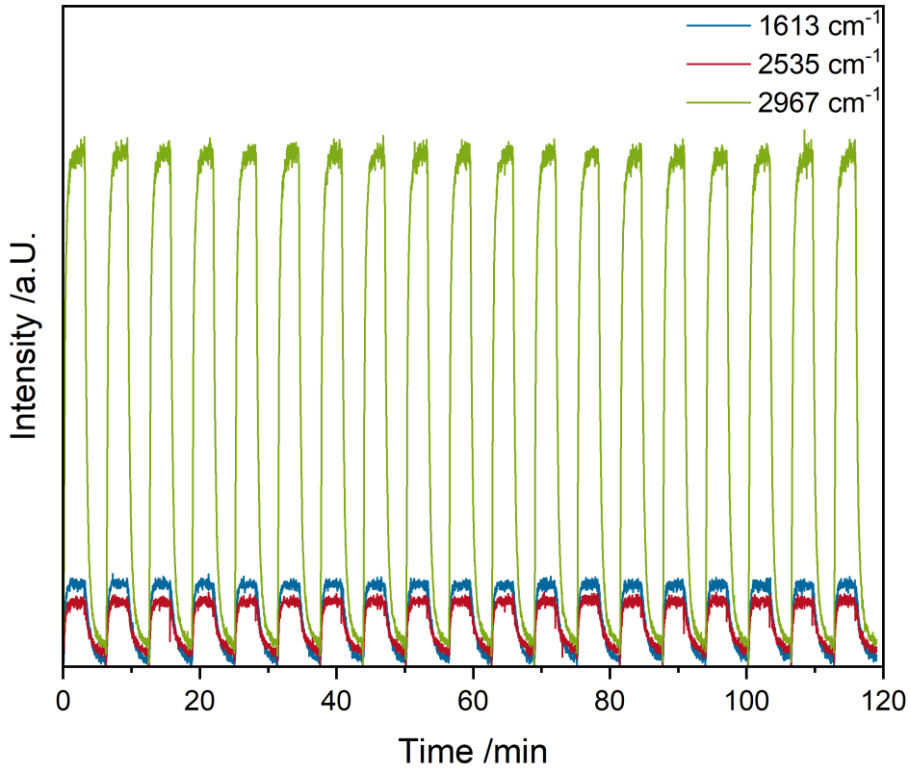

Figure S2: Course plot of an adsorbate, a background and a gas-phase position in the spectrum over the 20 measured periods to exclude period overarching effects during MES of the 1.2 V/nm² sample.

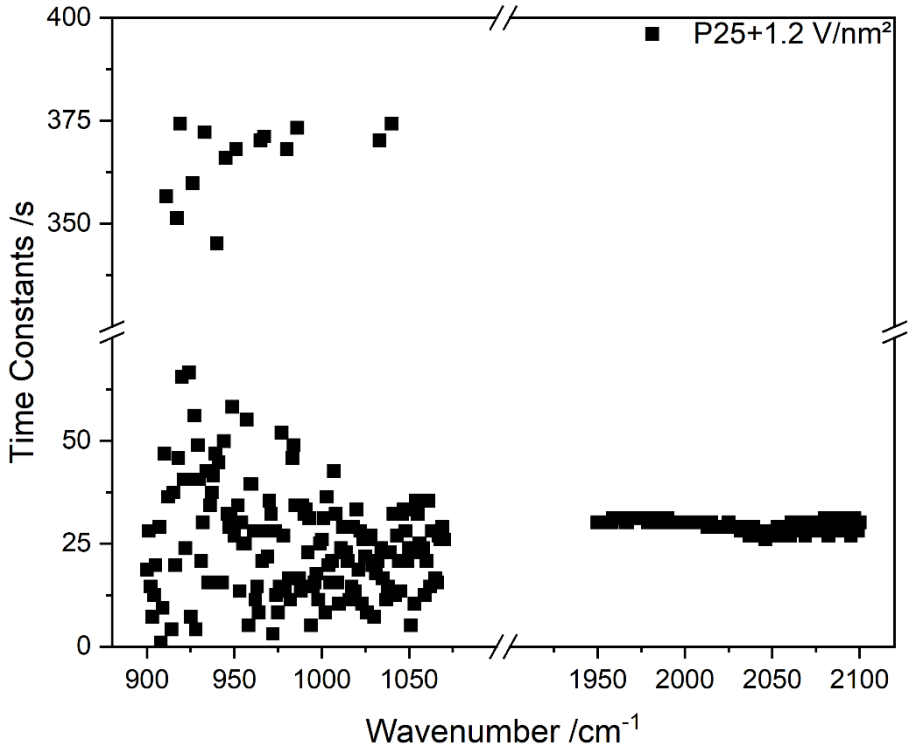

Figure S3: Screening of time constants determined by in-phase angle analysis of the 360° PSD spectrum of the P25+1.2 V/nm² sample in the vanadyl region within 900-1050 cm^{-1} and its overtone region within 1950-2100 cm^{-1}.

2) Additional Characterization Data

In the following, additional structural characterization data is given. In addition, a structural model for theSBA-15 based ALD synthesized $VO_x/TiO_2/SiO_2$ catalyst will be developed based on the data. XRD patterns and UV-Vis spectra for the TiO_2/SiO_2 and vanadia-loaded samples are shown in Figure S4.

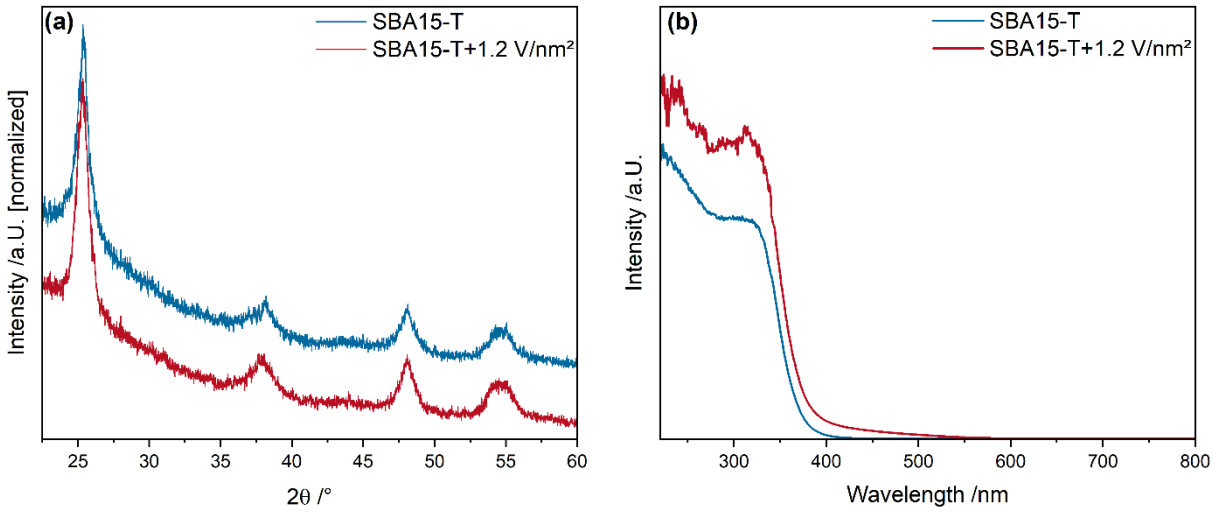

Figure S4: (a) XRD patterns and **(b)** UV-Vis spectra of ALD-synthesized $VO_x/TiO_x/SiO_2$ after 1 h of dehydration at 365 °C in 12.5% O_2/He and subsequent cooling to room temperature.

The UV-Vis spectra of the SBA-15-based samples show significant absorption contributions from titania in the region below 400 nm, indicating successful titania loading. The absorption is slightly lower than for bulk titania, which is explained by the smaller amount of TiO_2 present on the surface. The overall absorption below 400 nm increases when vanadia is loaded as the vanadia exhibits absorption in this region[1] and the TiO_2 conduction band is probably not perturbed by the V 3d orbitals anymore as it might be located at different energy values.[2] The relative amount of rutile present in the SBA15-T sample is much higher than for P25, which can be seen from the very pronounced absorption between 350 and 400 nm. The silica substrate itself does not show any significant absorption in this region.[2] Above 450 nm the TiO_2/SiO_2 sample shows, like bare P25, no significant absorption, whereas the vanadia-loaded SBA15-T shows a slight increase in the absorption, indicating the presence of some amount of polymerized vanadia on the surface.[1]

For the ALD synthesized TiO_2/SiO_2, the band gap is much larger than for P25, between 3.1 and 3.2 eV, which is much closer to the literature value of pure anatase and indicates a much less defective titania.[3] The SBA15-T+1.2 V/nm² sample is also in the same range and very similar to bare SBA15-T, which is in agreement with the behavior of P25 at the same loading. The TiO_2 crystallites for all ALD samples are small enough that their band gap energies might also be influenced by confinement effects of the TiO_2 nanoparticles, which makes the assignment of anatase and rutile amounts based on their band gap energy difficult.[4]

In comparison, the XRD patterns of the ALD synthesized $VO_x/TiO_2/SiO_2$ samples show much broader reflexes than the P25-based samples, which would correspond to crystallite sizes of ~5 nm and be in agreement with the observed band gap energies of above 3.0 eV. No distinct features of the rutile phase can be observed, indicating either a pure anatase phase, or the presence of rutile crystallites of <2 nm too small to be detected by XRD, which is likely the case, due to a strong absorption of the rutile position in UV-Vis spectra. For the SBA15-T samples, no changes are apparent between the bare sample and the vanadia-loaded one, indicating that only amorphous or nano crystalline vanadia is present on the surface.

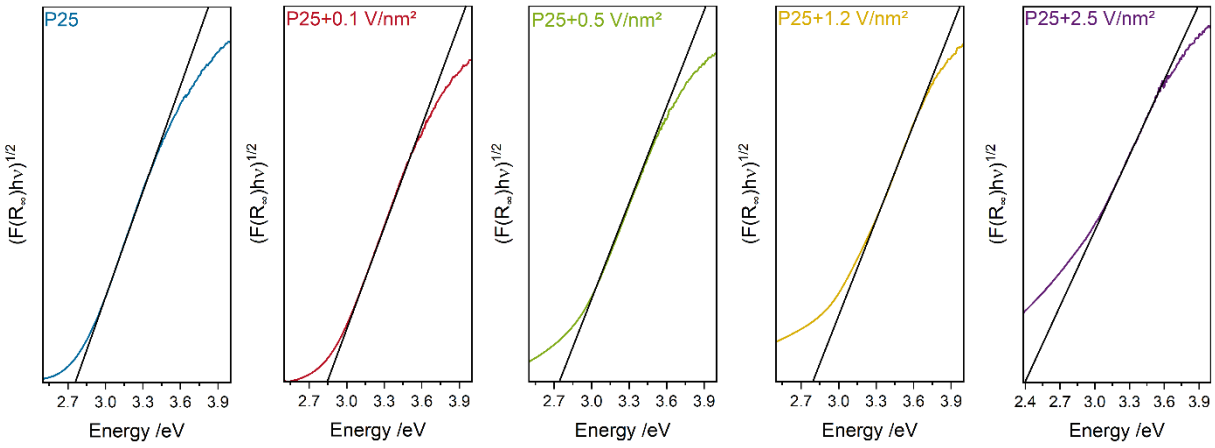

Figure S5: Tauc plots from room temperature spectra after dehydration (see Figure 1) of bare P25 and vanadia-loaded samples used for the determination of the band gap.

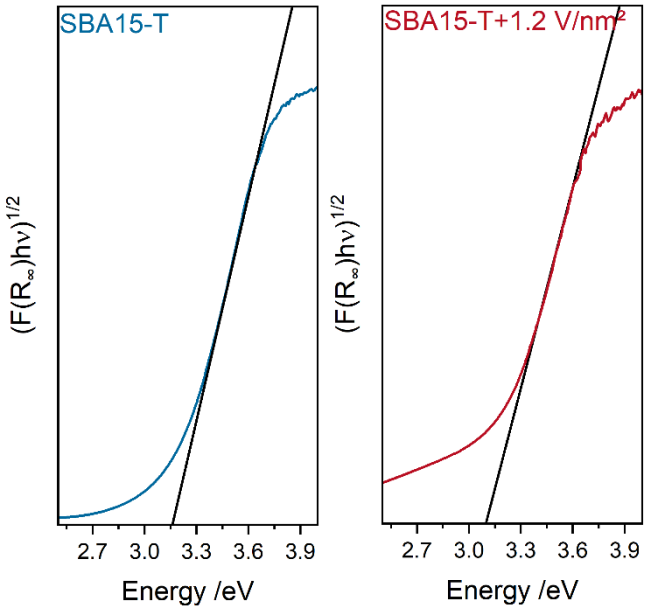

Figure S6: Tauc plots from room temperature spectra after dehydration (see Figure S2) of ALD-synthesized $VO_x/TiO_x/SiO_2$ used for the determination of the band gap.

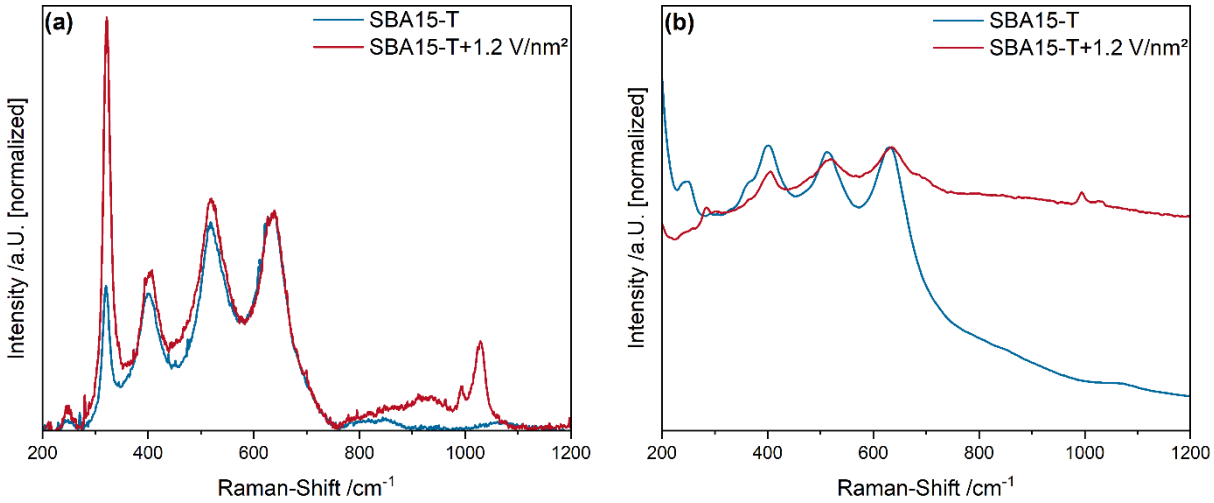

Figure S7: (a) UV-Raman (385 nm excitation) and **(b)** Vis-Raman (514 nm excitation) spectra of ALD-synthesized $VO_x/TiO_x/SiO_2$ after 1h of dehydration at 365 °C in 12.5% O_2/He and subsequent cooling to room temperature.

For ALD-synthesized titania samples, the same peaks as for P25-based samples are present, but the relative intensities are different. The Raman assignments are given in Table 3. The UV-Raman spectra of the ALD-synthesized samples (see Figure S7), show a larger relative amount of the rutile B_{2g} phonon than the P25 samples. This indicates that, despite the fact that the rutile crystallites in P25 are much larger (see

XRD in Figure S4), the overall amount of rutile close to the surface seems to be higher for the SBA15-T sample. The XRD patterns of the ALD-synthesized titania samples show no rutile reflexes, indicating very small rutile particles that are too small to be detected by XRD. This behavior is still in good agreement with the UV-Vis spectra, also showing higher relative amounts of rutile compared to bare P25. This can also explain why the intensities of the V=O and the V-O-V peak for the vanadia-loaded sample have a higher relative intensity (normalized to the anatase phase) compared to P25-based samples, as the high and very dispersed rutile content increases the vanadia mobility even further, to the point of large amounts of V-O-V being present even at lower loadings.[5] Additionally, the sample shows significant contributions from V_2O_5, even when its intensity is not selectively enhanced at 385 nm excitation.

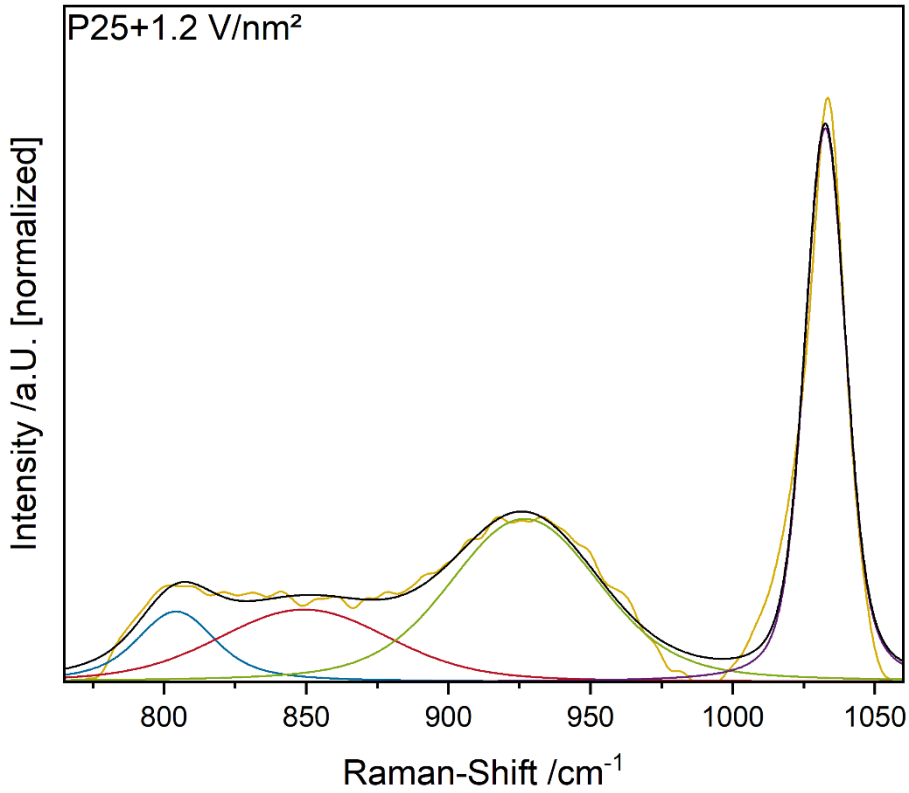

Figure S8: Exemplary fit of the vanadia region of P25+1.2 V/nm² from Vis-Raman spectra (514 nm excitation) after 1 h of dehydration at 365 °C in 12.5% O_2/He and subsequent cooling to room temperature.

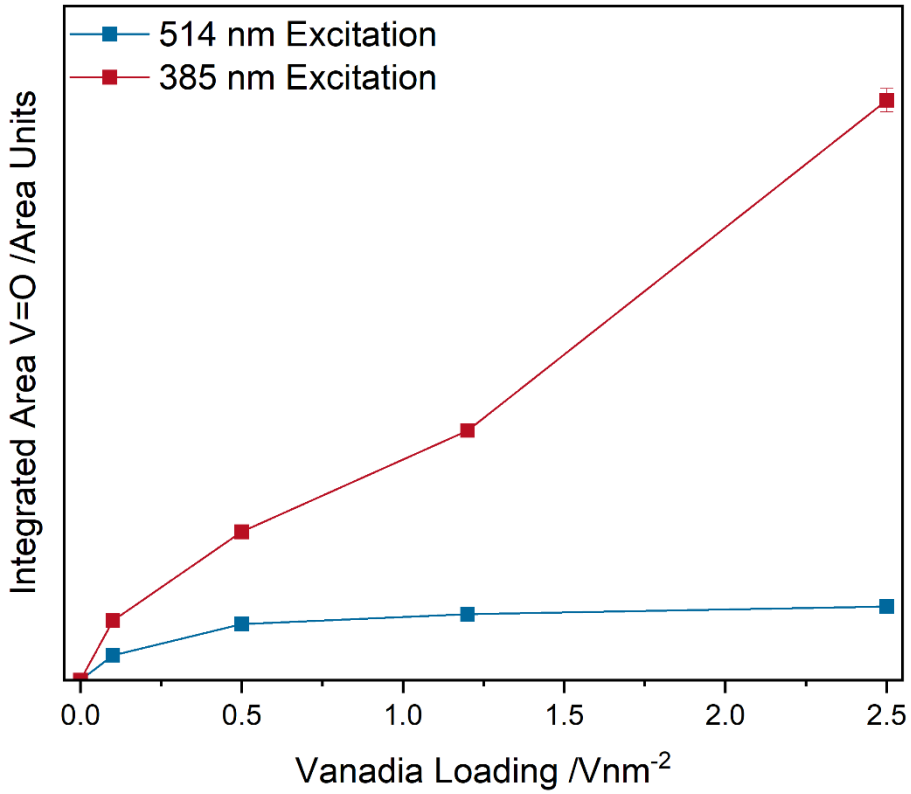

Figure S9: Integrated area of the vanadyl region from Raman spectra recorded after 1 h of dehydration in 12.5% O_2/He at 365 °C and subsequent cooling to room temperature, using 385 and 514 nm laser excitation.

Table S1: Surface composition of ALD synthesized TiO_x/SiO_2 and $VO_x/TiO_x/SiO_2$ samples and P25+1.2 V/nm² as a reference for bulk TiO_2 as determined by XPS analysis.

	Ti	O	V	Si	O/Ti	O/Si
P25+1.2 V/nm²	21.6	64.2	1.3	-	3	-
SBA15-T	16.5	68.3	-	7.1	4.1	9.6
SBA15-T+1.2 V/nm²	16.0	70.7	0.9	8.4	4.4	8.4

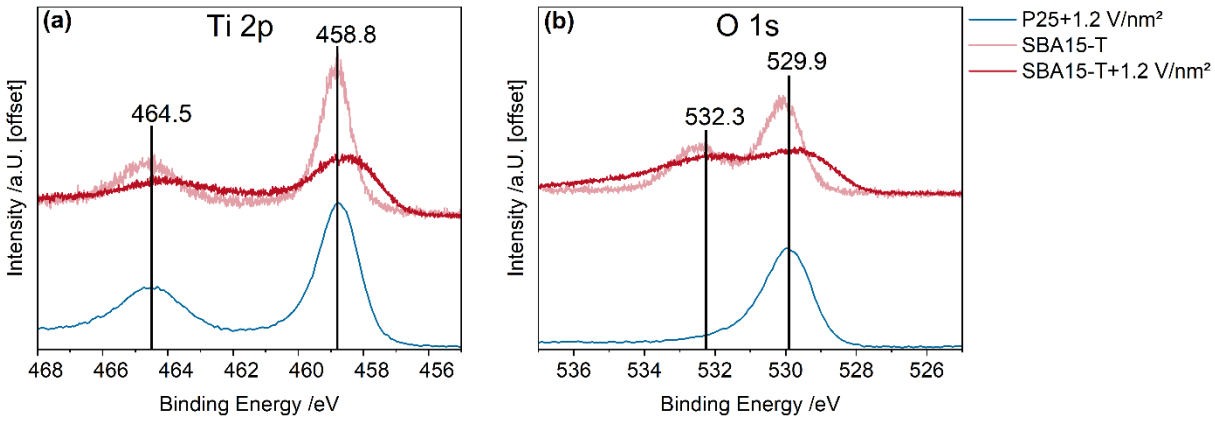

Figure S10: XP spectra of **(a)** the Ti 2p region and **(b)** the O 1s region of ALD synthesized TiO_x/SiO_2 and $VO_x/TiO_x/SiO_2$ and P25+1.2 V/nm² as a reference for bulk TiO_2. The positions of the P25 peaks are marked as a reference for the ALD synthesized samples.

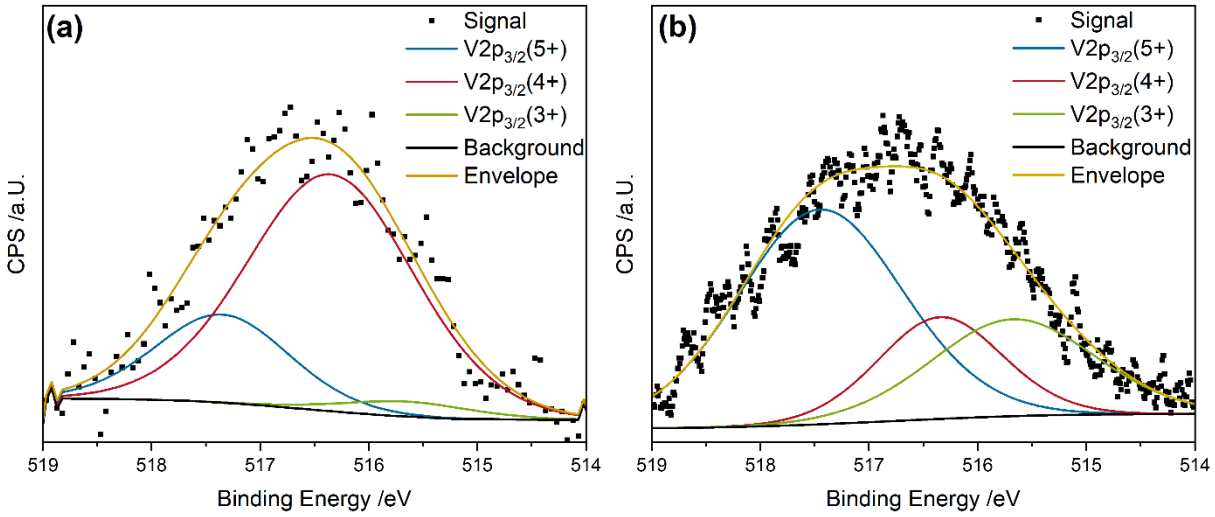

Figure S11: $V2p_{3/2}$ photoemission of P25+1.2 V/nm² **(a)** and $VO_x/TiO_x/SiO_2$ **(b)** at room temperature together with the results of a fit analysis with three components representative of different vanadium oxidation states.

Table S2: Summary of the distribution of vanadium oxidation states for P25+1.2 V/nm² and $VO_x/TiO_x/SiO_2$ samples, based on a fit analysis of the XP spectra shown in Figure 10.

	V^{5+}	V^{4+}	V^{3+}	V Average
P25+1.2 V/nm²	19.4	74.8	5.7	4.1
SBA15-T+1.2 V/nm²	55.6	19.7	24.7	4.3

To further characterize the structure of the ALD-synthesized samples and to propose a structure model, XPS and nitrogen physisorption experiments were performed. The elemental compositions, determined from XP survey spectra, are summarized in Table S1. P25+1.2 V/nm² was measured as a bulk titania reference sample with the same vanadia surface density. The bulk titania shows only three elements, besides ubiquitous carbon, on the surface, indicating that there are no further impurities. The amount of vanadium is in line with the expected value for the surface density. Notably, the stoichiometry of oxygen to titania is not 2:1 but rather much higher, indicating that oxygen is more concentrated on the surface when vanadia is present. In comparison, the samples based on SBA-15 show not only significant amounts of titania on the surface, indicating successful coating, but also silicon, indicating that the titania was probably deposited as a layer during ALD but formed islands during the crystallization process, resurfacing some of the SiO_2 sites. For the TiO_2/SiO_2 sample, this is a well-known behavior and had been observed previously.[6] As there were no Si-O-V bonds visible in UV-Raman spectroscopy, and vanadia is bound much more strongly to titania than to silica, it can be assumed that vanadia is located fully on the titania support. The preferential binding of vanadia to titania in comparison to other supports had already been observed in Raman spectroscopy and supported by DFT in the literature.[7–9] As the surface area and surface density of the SBA15-T+1.2 V/nm² is similar, but the titania is only present in islands on the SBA-15, vanadia needs to be very close together on the islands. This explains, why the V-O-V and V=O signals of the SBA15-T+1.2 V/nm² samples are much more intense in UV-Raman spectra (see Figure S7) than for the P25 samples.

Detailed XP spectra for the Ti 2p region (see Figure S9a) reveal that P25 is mostly present in Ti^{4+} states at 458.8 eV and only has a very small contribution from Ti^{3+} states at lower binding energies.[10,11] The surface appears to be much less

defective than suggested by the measured band gap energies (see Figure 1b), which indicates a more significant amount of defects in the titania lattice instead of at the surface. This leads to the conclusion that most of the Ti^{3+} defective states are probably located in the subsurface/bulk region of the lattice, which is maybe facilitated by surface vanadia. In comparison the TiO_2/SiO_2 sample shows similar peak shapes and positions to P25+1.2 V/nm². When the sample is loaded with vanadia, the intensity of the peaks decreases. As vanadia is located only on the titania islands, the effective amount of titania detected by XPS is decreased, as the signal now also needs to cross through the vanadia layer. Furthermore, for SBA15-T+1.2 V/nm² there is a significant increase in the intensity at lower binding energies indicative of Ti^{3+} states,[11] which means that the titania on SBA15-T becomes more defective upon vanadia impregnation. This high number of defective states is not in agreement with UV-Vis band gap energies, as they indicate a high degree of non-defective TiO_2. The titania is likely to have not fully crystallized after ALD impregnation so that a large amount of titania is amorphous, which can be highly defective, whereas the parts of the titania islands that are present in a crystallized form are defect free. When the O1s detailed spectra (see Figure S9b) are considered, the P25+1.2 V/nm² sample shows an O1s centered around 529.9 eV, representative of oxygen in the TiO_2 lattice.[11] Additionally, the peak shows a slight asymmetry towards higher binding energies, which is likely to be caused by defective Ti^{3+} states. During the creation of a defect, a charge transfer from the oxygen to the titania occurs, thereby increasing the binding energy of the oxygen and decreasing the binding energy of titania.[11] For the ALD-synthesized samples, an additional signal for oxygen from SiO_2 is located at 533 eV.[12] On the bare titania sample, significant contributions from Ti-OH species can be detected at 532.2 eV,[10,13] which decrease significantly upon vanadia impregnation, indicating that vanadia is anchored to the titania at Ti-OH sites. Additionally, the O1s signal is much broader, indicating the presence of varied oxygen species in the titania samples, which is in good agreement with the assumption of large amounts of amorphous and defective titania through the ALD synthesis.

Detailed spectra of vanadium were fitted using three components, representing the different oxidation states of vanadium. The relative contributions of each oxidation state to the overall V2p signal are summarized in Table S2. For the P25+1.2 V/nm² sample, a large amount of V^{4+} is present, while the remaining vanadium atoms are mostly present in the V^{5+} state. In comparison, the ALD synthesized samples have a

higher amount of V^{5+} species, which represents more than half of the overall species. On the other hand, these samples also have a much larger contribution from V^{3+} states, indicating a high degree of disorder in the vanadia states but an overall higher average oxidation state of ~4.35 in comparison to 4.14 on P25. As only vanadia with vanadium in oxidation state V^{5+} has a significant Raman scattering cross section, the oxidation state distribution in these samples also explains the more intense signal of vanadia-related features in the Raman spectra.

Table S3: Specific surface areas and pore diameters from nitrogen physisorption and subsequent BET analysis before and after TiO_2 coating by ALD.

	SBA15-T	
	Surface Area /m^2g^{-1}	Pore Diameter /nm
Before TiO_2 Coating	697.5	8.1
After TiO_2 Coating	78.0	3.6

Finally, the specific surface areas and average pore diameters of the silica and the TiO_2/SiO_2 sample were determined by nitrogen physisorption and BET analysis: the results are summarized in Table S3. The specific surface area and the average pore diameter of the SBA-15 decrease significantly from 697.5 to 78.0 m^2/g and 8.1 to 3.6 nm, respectively. This is indicative of a blocking of the SBA-15 pores during the ALD process through the deposited titania, which was observed previously and is in good agreement with our XPS data.[6] The titania agglomerates on the pores, which are, on average, too small to allow for the formation of larger titania crystallites. Therefore, the deposited titania sits on top of the pores and creates a much smoother SBA-15 surface. The rough silica at the edge between the surface and the pores might also lead to large amount of amorphous and defective titania that could be determined from the Ti 2p XP spectra. To summarize the structural information on the ALD synthesized samples, a scheme is presented in Figure S11. The vanadia structure is not further specified as the structure is similar to that on P25 (from Raman and UV-Vis analysis), but with a higher degree of oligomerization.

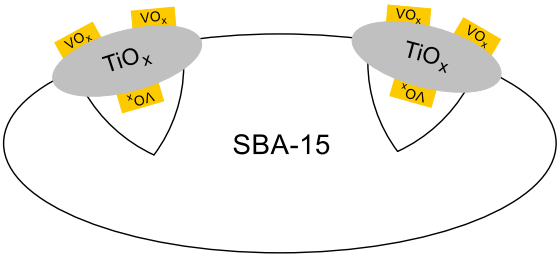

Figure S12: Proposed structure for the $VO_x/TiO_2/SiO_2$ sample on silica SBA-15, based on multiple characterization methods.

3) Operando Spectroscopic Data

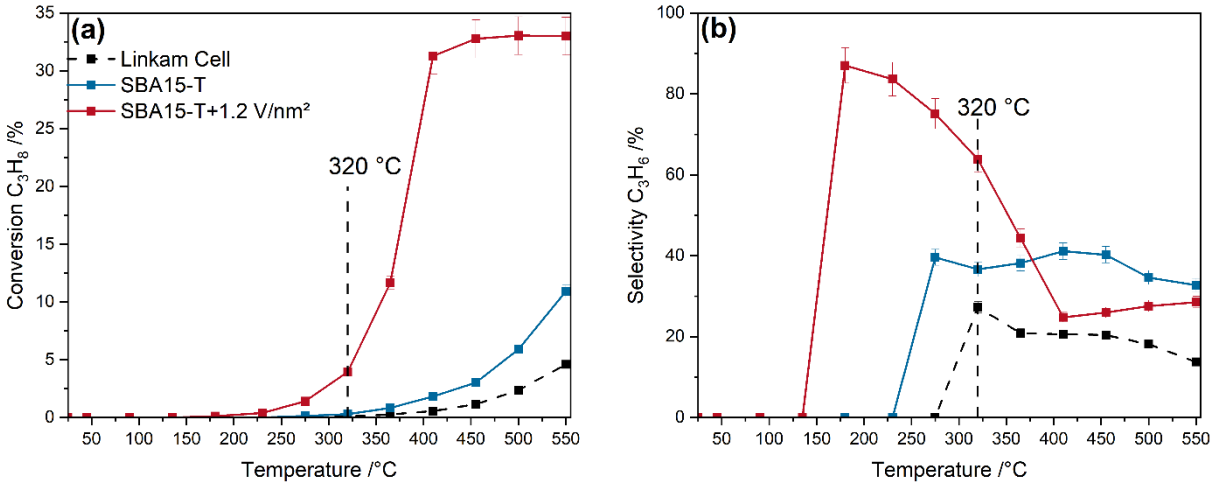

Figure S13: (a) Propane conversions and **(b)** propylene selectivities of the ALD synthesized TiO_x/SiO_2 and $VO_x/TiO_x/SiO_2$ samples as well as for the empty reaction cell as a reference. The temperature at which operando spectroscopy was performed is marked.

To compare the much lighter ALD synthesized samples to the bulk P25 samples, the conversions are normalized to the surface area of the catalysts, resulting in conversion per m². After that, the observed behavior of the conversions for the ALD-synthesized samples is very similar to that for P25, but the selectivities are significantly larger. At 320 °C, the conversions are lower for the ALD-synthesized samples than for P25, but the selectivity of SBA15-T+1.2 V/nm² in particular is much larger, which can be explained well by the lower conversion. Overall, the behavior is similar to the P25-based samples. The lower conversion can be caused by the fact that the titania film grew over the SBA-15 pores, which would cause some of the subsequently loaded vanadia to be located in the pores with limited access to the gas-phase through the titania film. The lower conversion explains the increased selectivity.

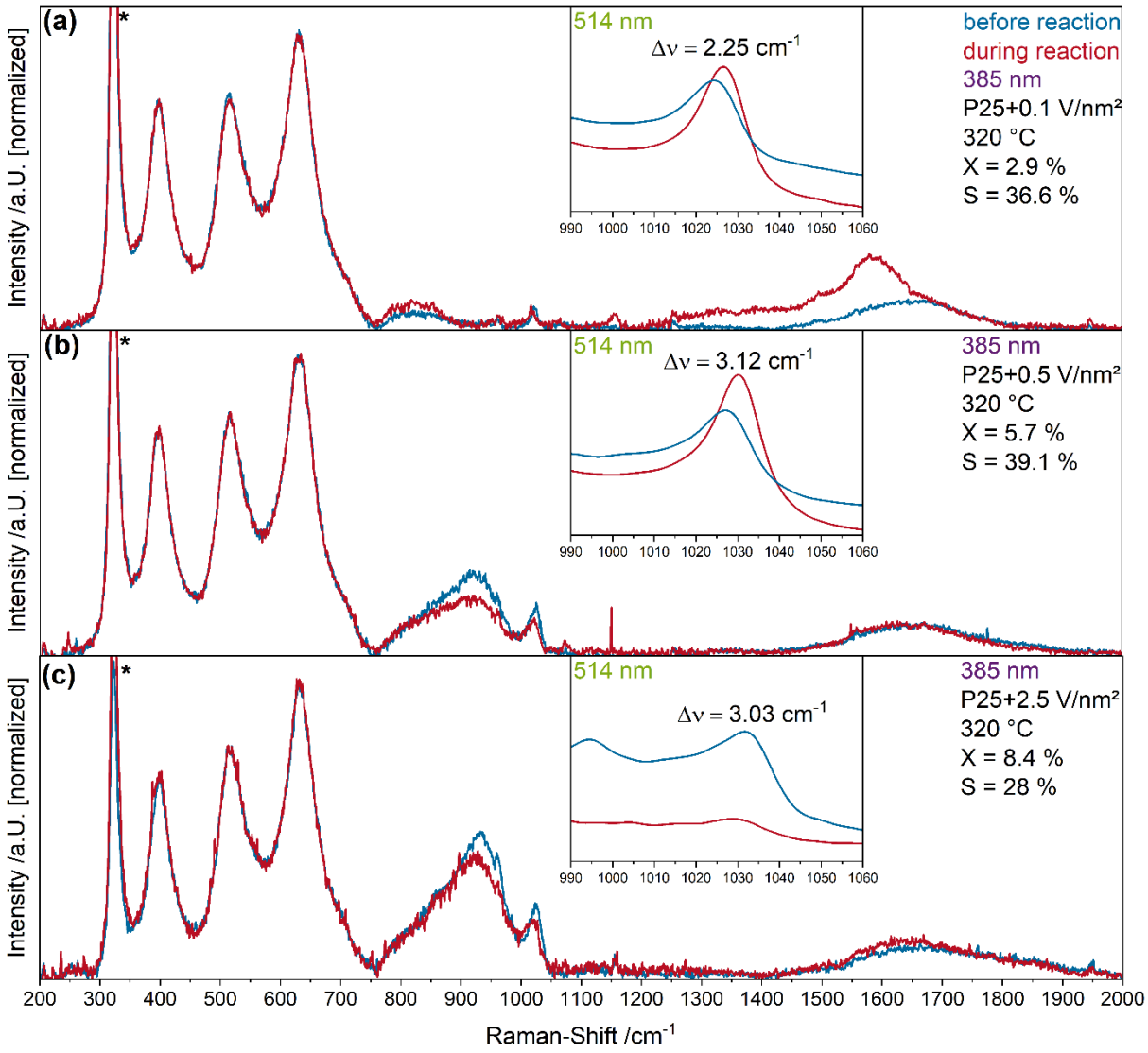

Figure S14: Normalized operando UV-Raman (385 nm excitation) spectra of **(a)** P25+0.1 V/nm², **(b)** P25+0.5 V/nm², and **(c)** P25+2.5 V/nm² recorded at 320 °C under oxidizing (blue; 12.5% O_2/He) and reactive conditions (red; 12.5% O_2/12.5% C_3H_8/He), characterized by the given conversions and selectivities. The insets show the corresponding Vis-Raman spectra (514 nm excitation) of the vanadyl region together with the shift of the vanadyl position. The spectra are normalized and the peak originating from the used CaF_2 window is marked with an asterisk.

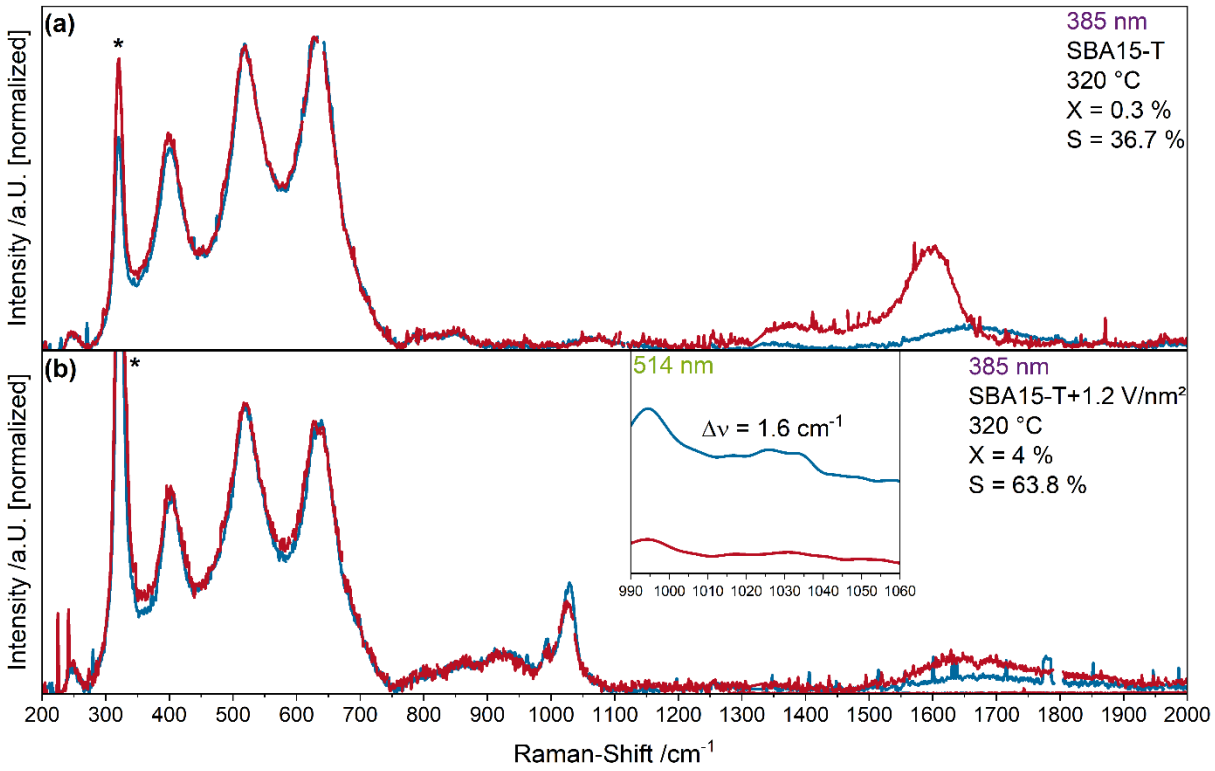

Figure S15: Normalized operando UV-Raman (385 nm excitation) spectra of **(a)** SBA15-T and **(b)** SBA15-T+1.2 V/nm² recorded at 320 °C under oxidizing (blue; 12.5% O_2/He) and reactive conditions (red; 12.5% O_2/12.5% C_3H_8/He), characterized by the given conversions and selectivities. The insets show the corresponding Vis-Raman spectra (514 nm excitation) of the vanadyl region together with the shift of the vanadyl position. The spectra are normalized and the peak originating from the used CaF_2 window is marked with an asterisk.

For the ALD-synthesized samples, the deposition of carbon is the main structural change, similar to P25. The changes in the rutile B_{2g} mode are also present, but to a lesser degree. When quantifying the structural dynamics, both the increase in rutile and the deposited carbon correlate well with the conversions of the samples (compare Figure S12). For SBA15-T+1.2 V/nm², the V-O-V dynamics are not as clearly defined as for the P25 samples and a decrease in the vanadyl intensity is the main structural dynamic, which is also in agreement with the small shift in the vanadyl peak observed in Vis-Raman spectroscopy. Notably, the amount of vanadium detected for the ALD-synthesized samples by XPS is 50% lower than for the P25 samples at the same loading but they have 2.85 times the amount of V^{5+}. As only V^{5+} species have a good Raman scattering cross section,[14] both of these factors influence the amount of Raman signal, leading to about 1.5 times the expected Raman signal in comparison to P25 samples at the same loading. Nevertheless, structural factors such as the higher

degree of oligomerization (compared with XPS results) leads to an increased vanadia signal at the same loading.

The vanadia-related dynamics, especially the V-O-V dynamics, are less intense than for P25 but the observed conversions are also smaller, which is in good agreement. Additionally, the higher amount of V^{5+} on this sample might lead to the higher selectivity, as reduced vanadia species were previously proposed to be less active.[5,15]

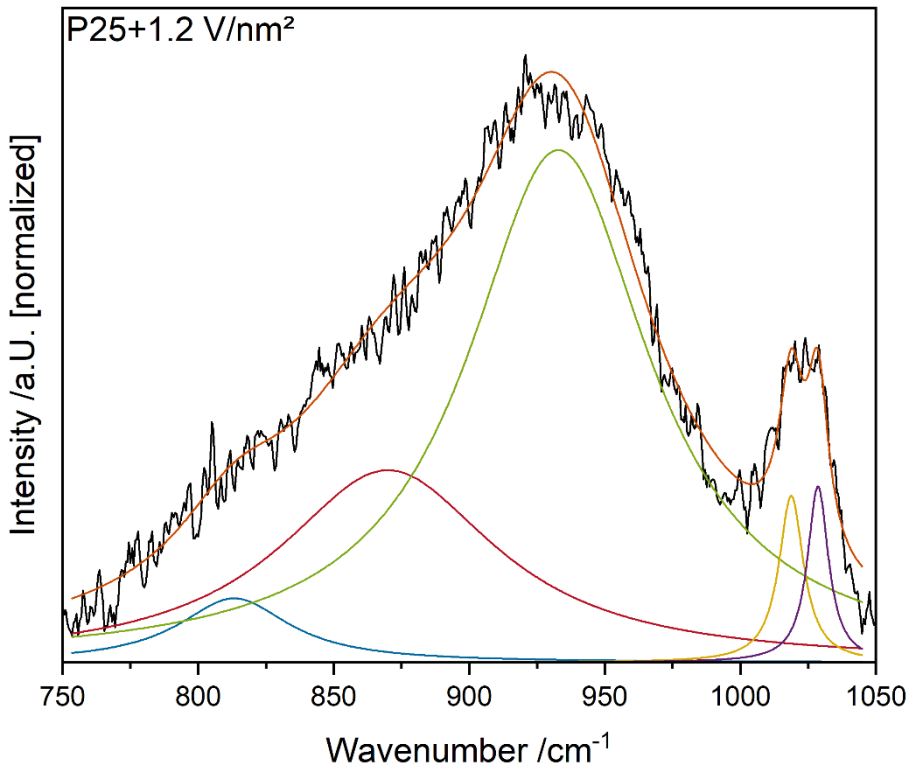

Figure S16: Exemplary fit analysis of the vanadia-related region in the UV-Raman (385 nm excitation) spectrum of the P25+1.2 V/nm² sample. The vanadyl peak was fitted with a monomeric and a dimeric component.

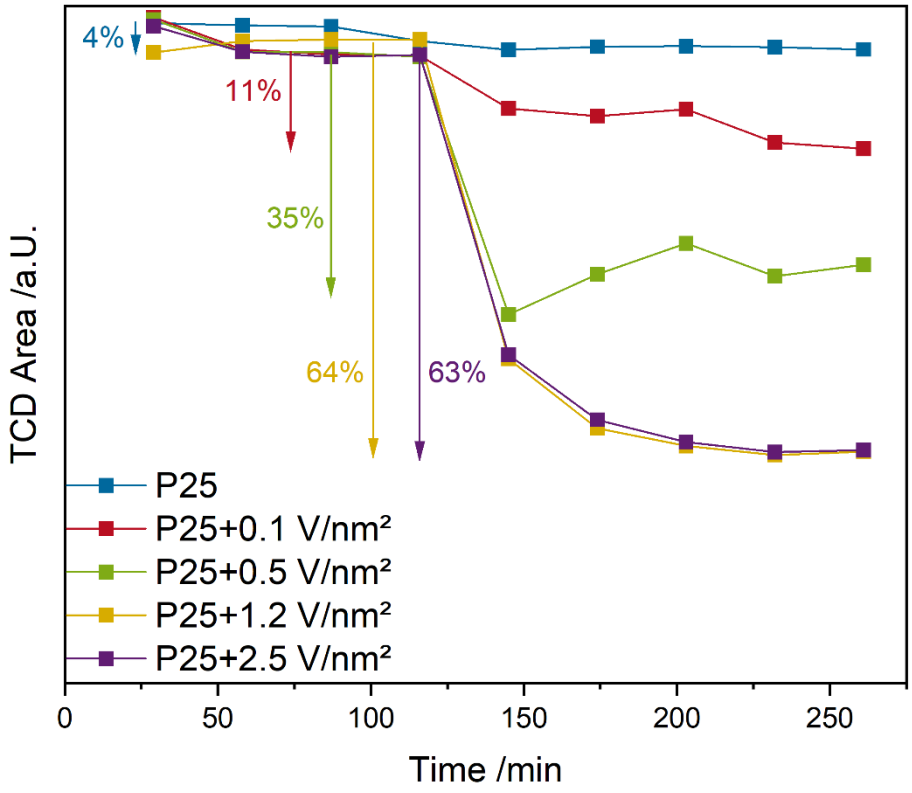

Figure S17: Oxygen traces as determined by the thermal conductivity detector (TCD) for the P25-based samples under oxidizing (12.5% O_2/He) and reactive (12.5% O_2/12.5% C_3H_8/He) conditions. The arrows indicate the percentage of converted oxygen for each sample.

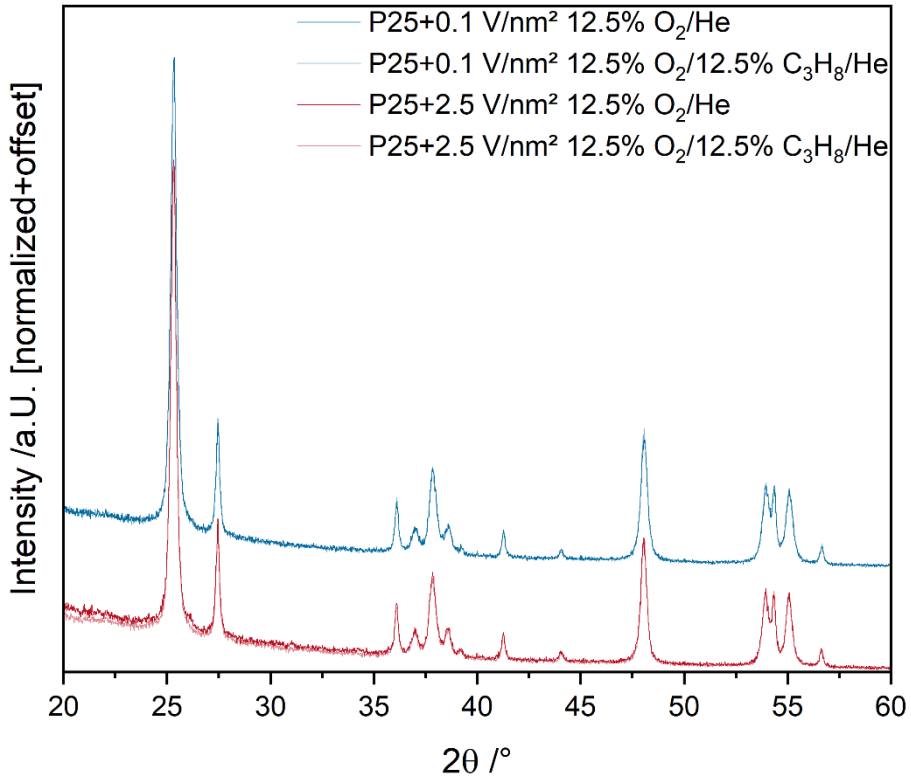

Figure S18: Operando XRD patterns of P25 loaded with 0.1 and 2.5 V/nm² recorded during reactive (12.5% O_2/He) and oxidative (12.5% O_2/12.5% C_3H_8/He) conditions at 320 °C.

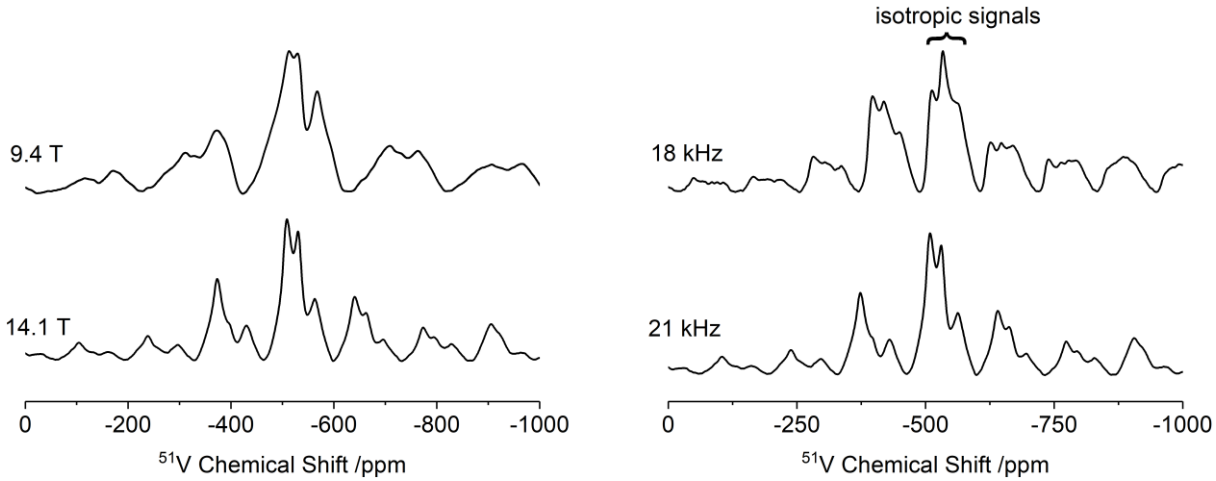

Figure S19: ^{51}V ssNMR spectra of P25+1.2 V/nm² measured at 9.4 and 14.1 T, respectively, and 21 kHz spinning (left side). The broadening of the signals in the 9.4 T spectrum indicate the presence of second-order quadrupolar interactions. Comparison of spectra obtained at 14.1T using different spinning rates of 18 and 21 kHz (right side) to identify the positions of the isotropic signals.

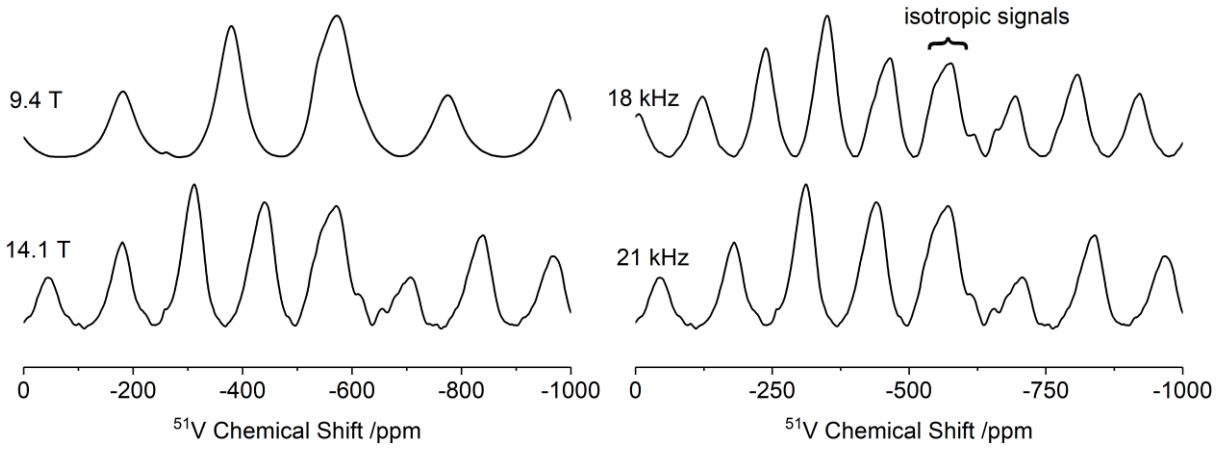

Figure S20: ^{51}V ssNMR spectra of CeO_2+1.2 V/nm² measured at 9.4 and 14.1 T, respectively, and 21 kHz spinning (left side). The broadening of the signals in the 9.4 T spectrum indicate the presence of second-order quadrupolar interactions. Comparison of the spectra obtained at 14.1 T using two different spinning rates of 18 and 21 kHz (right side) to identify the positions of the isotropic signals. The VO_x/CeO_2 sample was measured as a reference to validate our methods, as the vanadia nuclearity distribution is already known from the vanadyl peak and can be compared for oligomeric signals.

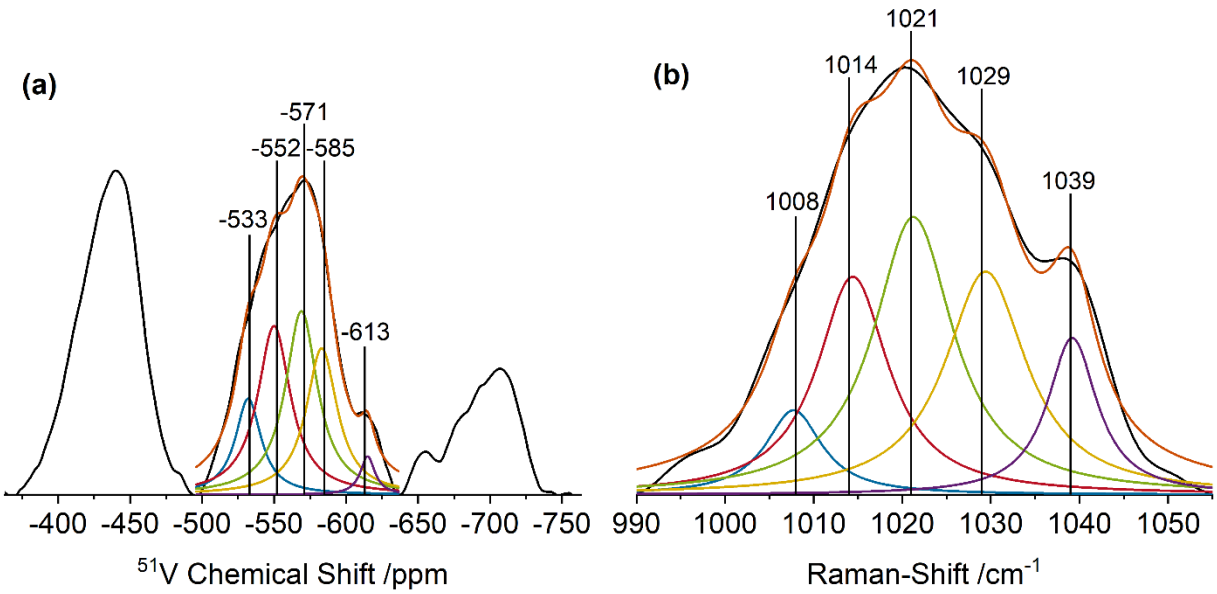

Figure S21: (a) Deconvolution of the isotropic signal in the ^{51}V ssNMR of VO_x/CeO_2 measured at 14.1 T and 21 kHz spinning, compared to **(b)** the vanadyl region of the same sample from Vis-Raman (514 nm excitation) spectroscopy. The positions of the different vanadia species are marked.

Table S4: Assignments of the vanadium positions in ^{51}V ssNMR spectroscopy[16] and the vanadyl peaks in Vis-Raman spectroscopy (514 nm excitation).[17]

^{51}V ssNMR		**UV-Raman**	
Chmical Shift /ppm	Assignment	Raman-Shift /cm^{-1}	Assignment
-533	Monomeric vanadia	1008	Monomeric vanadia
-552	Dimeric vanadia	1014	Dimeric vanadia
-571	Dimeric vanadia	1021	Trimeric vanadia
-585	Oligomeric vanadia	1029	Tetrameric vanadia
-613	Oligomeric Vanadia	1039	Oligomeric vanadia

For the SBA15-T+1.2 V/nm² sample, the overall amount of vanadyl oxygen as well as the contribution from dimeric species is higher than for P25+1.2 V/nm² but, as seen from the operando UV-Raman analysis (see Figure 4d), both V-O-V and the vanadyl oxygen are less active than for P25 samples, which is in good agreement with the decreased conversion. This might be caused by the very irregular growth of titania and vanadia into the pores of the SBA-15 (see characterization section), which further confirms that some active sites have no contact with the gas-phase. As the titania

islands are still very thin, both NMR as well as UV-Raman should be integral methods for those sites, despite the fact that not all of them are active.

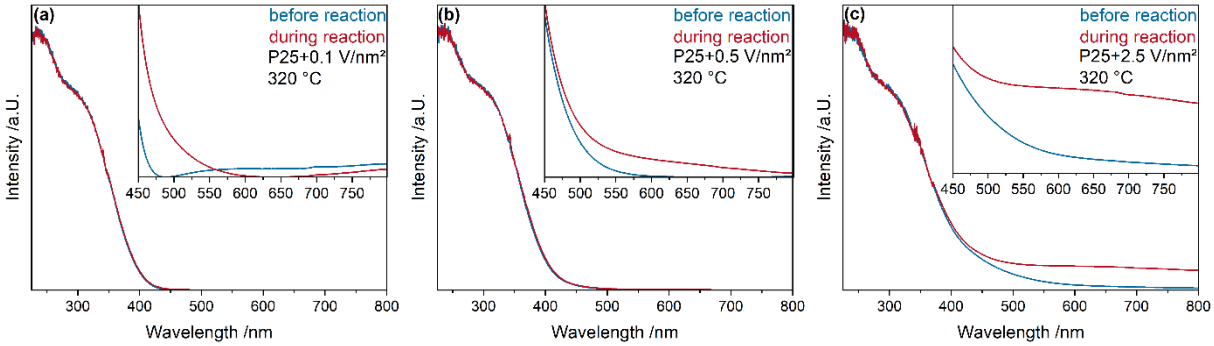

Figure S22: UV-Vis spectra of **(a)** P25+0.1 V/nm², **(b)** P25+0.5 V/nm², and **(c)** P25+2.5 V/nm² measured at 320 °C under oxidizing (blue; 12.5% O_2/He) and reactive conditions (red; 12.5% O_2/12.5% C_3H_8/He). The insets give an enlarged view of the visible region.

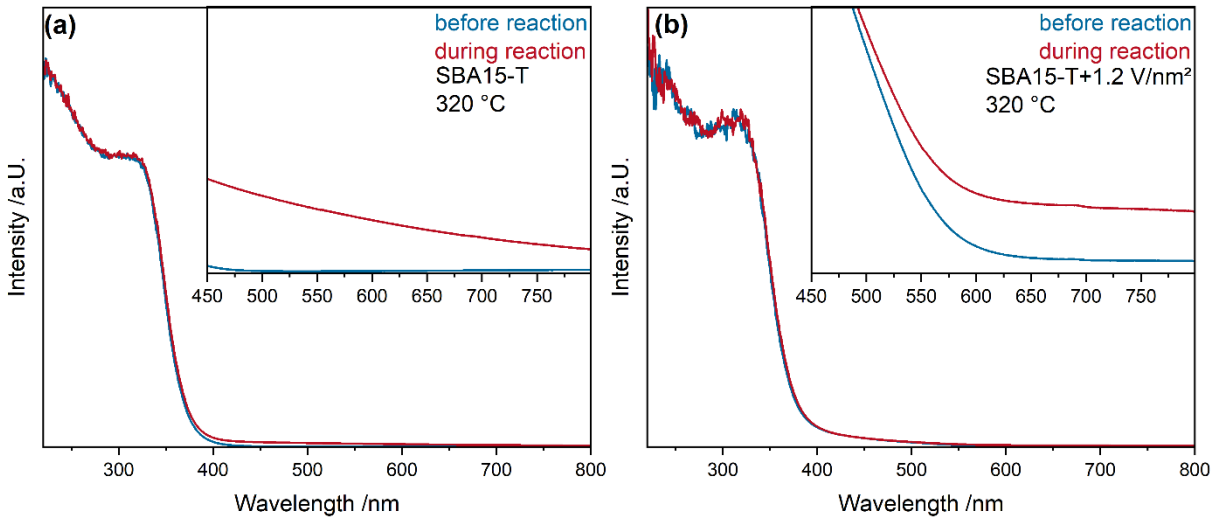

Figure S23: UV-Vis spectra of **(a)** SBA15-T and **(b)** SBA15-T+1.2 V/nm² measured at 320 °C under oxidizing (blue; 12.5% O_2/He) and reactive conditions (red; 12.5% O_2/12.5% C_3H_8/He). The insets give an enlarged view of the visible region.

The SBA15-T+1.2 V/nm² shows less intense vanadia d-d transitions, which is in agreement with the lower conversions compared to the P25 sample at the same surface density as well as the higher amount of vanadia in the V^{5+} state (compare XPS), which is maybe regenerated quickly from a reduced state, back towards the fully oxidized state, leading to more V^{5+} and therefore fewer d-d transitions.

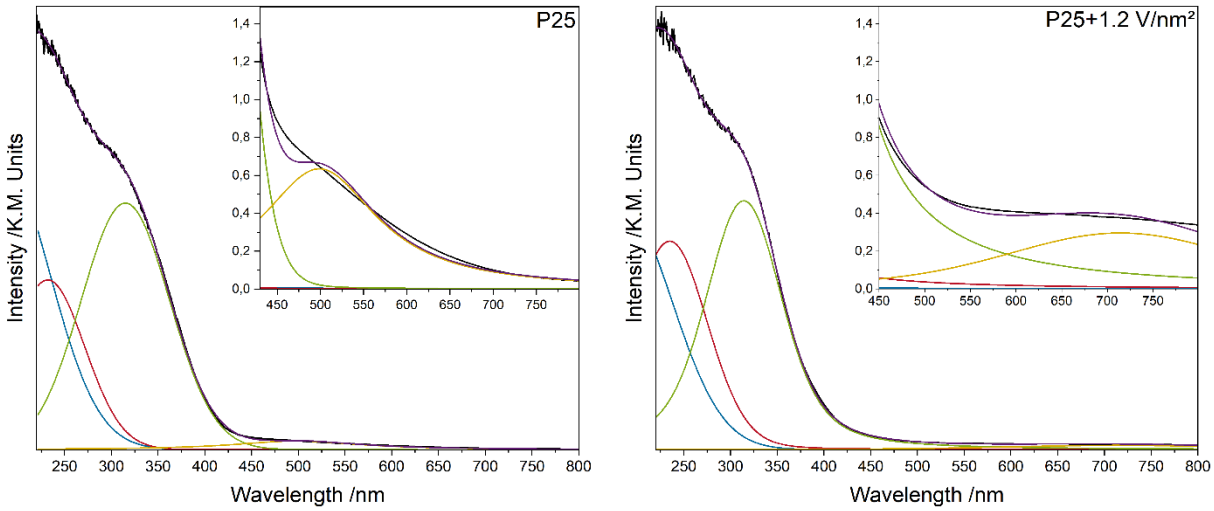

Figure S24: Exemplary fit of the UV-Vis spectra of P25 and P25+1.2 V/nm² at 320 °C during reaction conditions (12.5% O_2/12.5% C_3H_8/He).

4) Transient DRIFTS Data

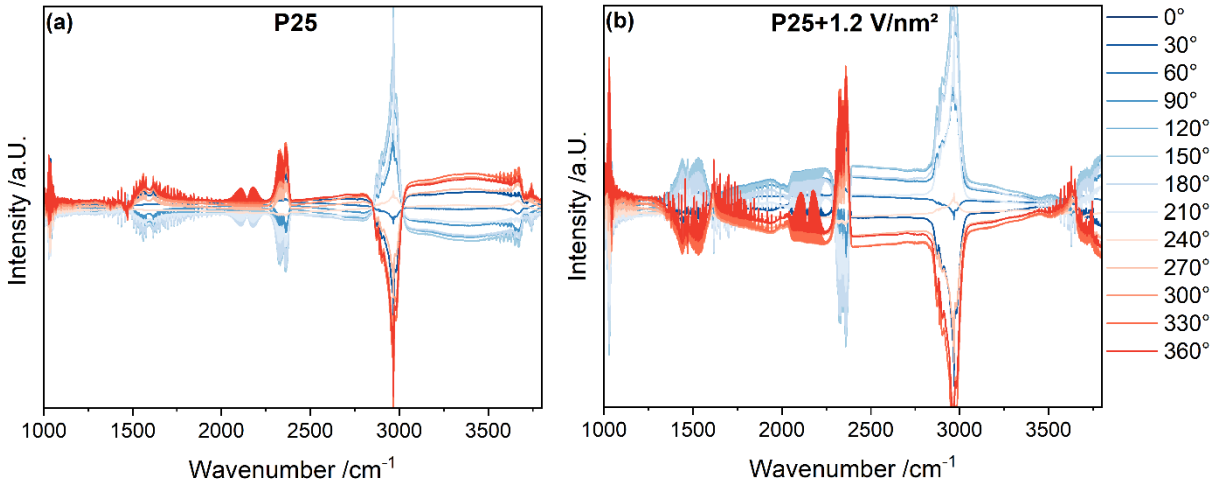

Figure S25: Phase sensitive detection (PSD) of DRIFT spectra of P25 and P25+1.2 V/nm², recorded during pulsed oxygen and constant propane flow, between 0° and 360° phase-shift in 30° steps.

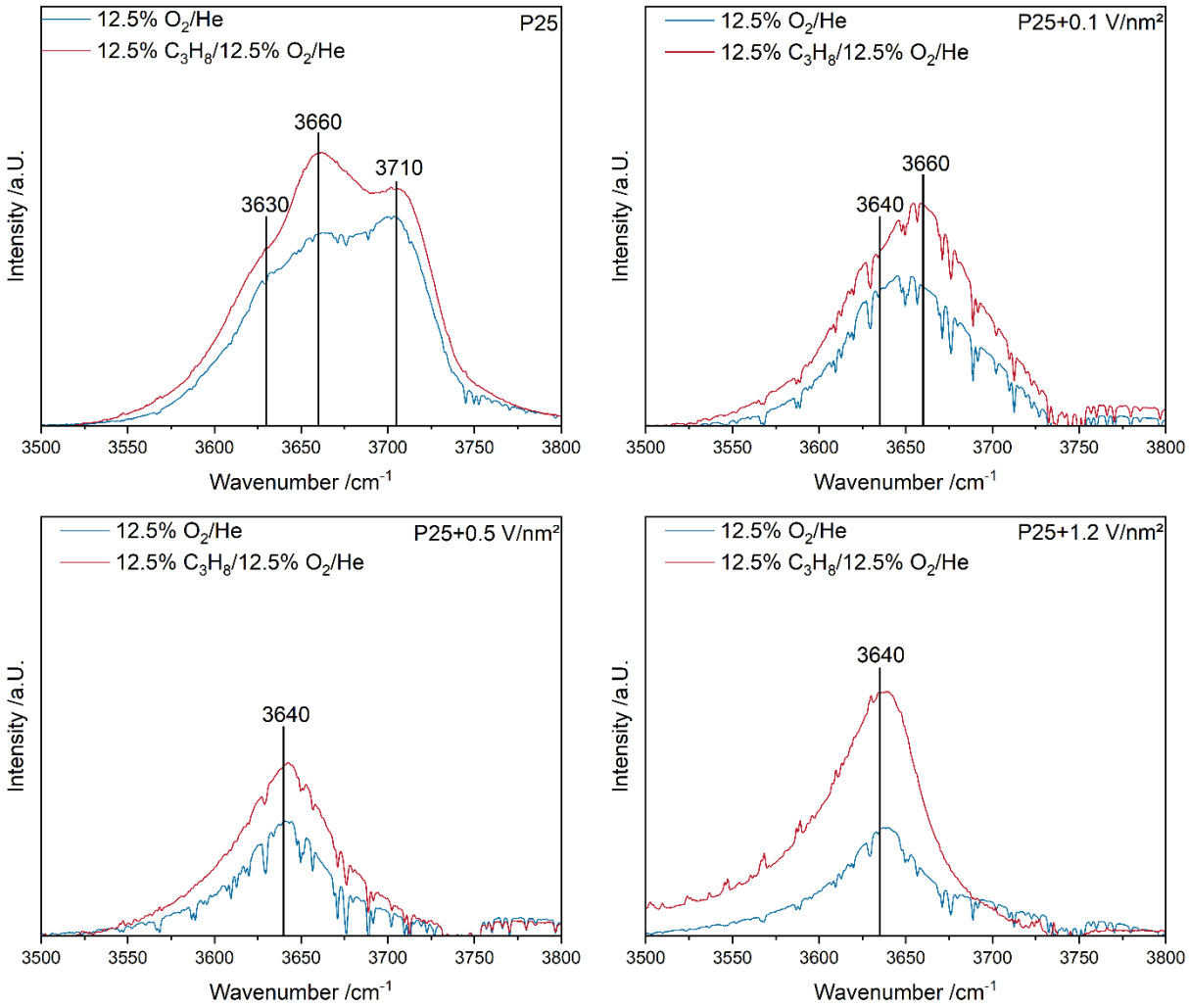

Figure 26: Static DRIFT spectra of the Ti-OH region of bare and vanadia-loaded P25 during reactive (12.5% O_2/12.5% C_3H_8/He) and oxidizing (12.5% O_2/He) conditions at 320 °C. The Ti-OH positions are marked.

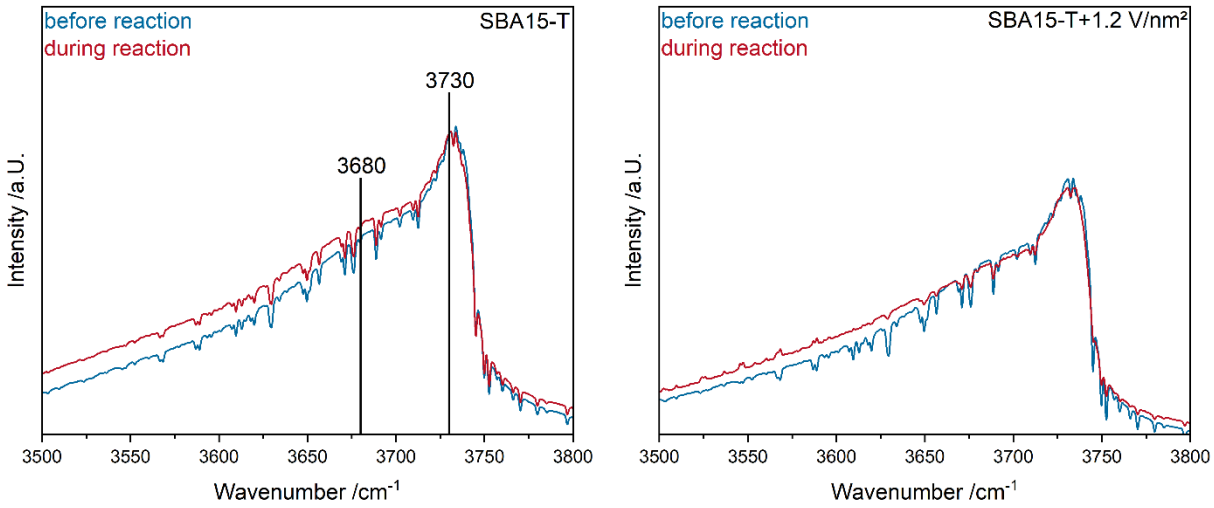

Figure 27: Static DRIFT spectra of the Ti-OH region of the ALD synthesized TiO_x/SiO_2 and $VO_x/TiO_x/SiO_2$ samples under reactive (12.5% O_2/12.5% C_3H_8/He) and oxidizing (12.5% O_2/He) conditions at 320 °C. The Ti-OH positions are marked.

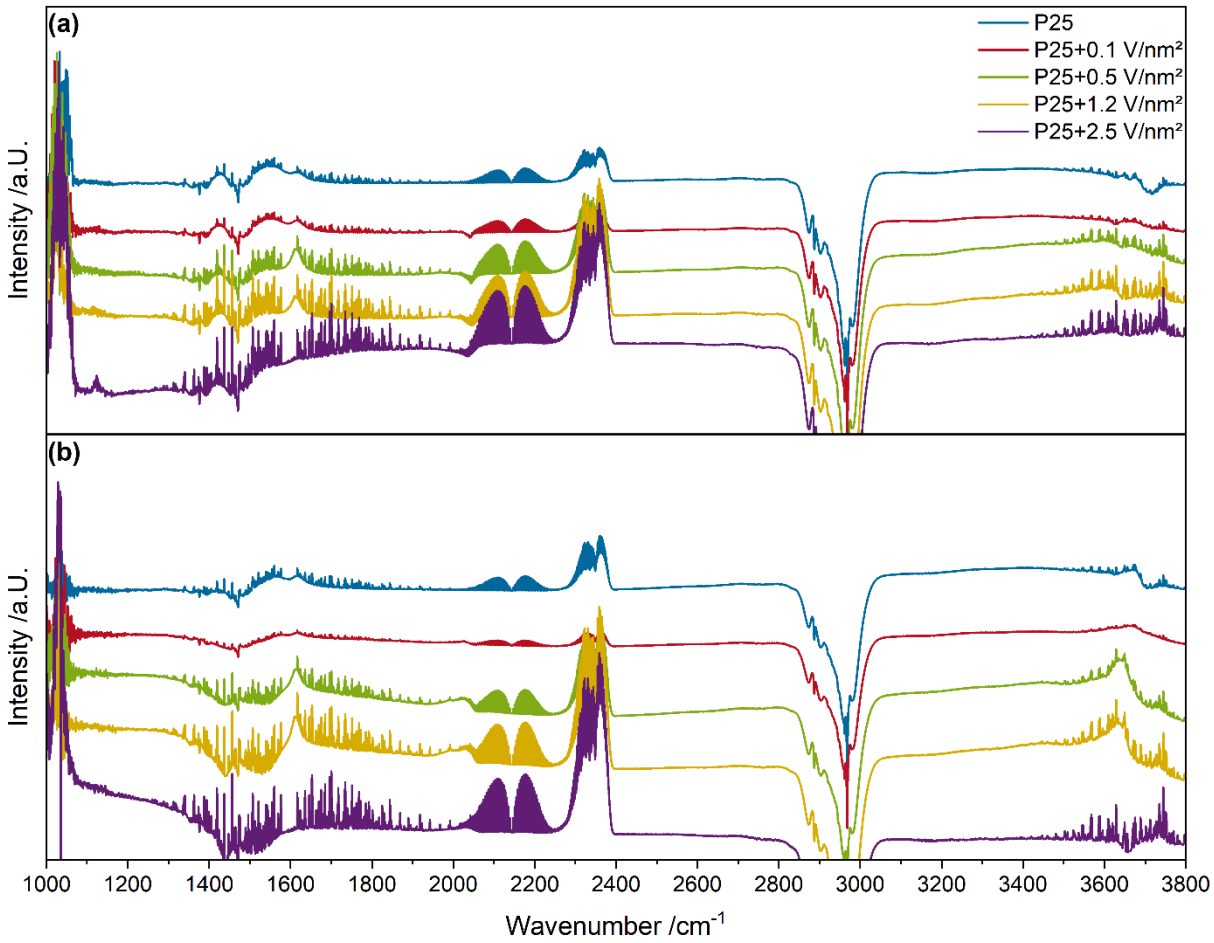

Figure S28: PSD spectra of P25 and vanadia-loaded P25 samples at a phase shift of 360° during **(a)** constant oxygen and pulsed propane flow and **(b)** constant propane and pulsed oxygen flow.

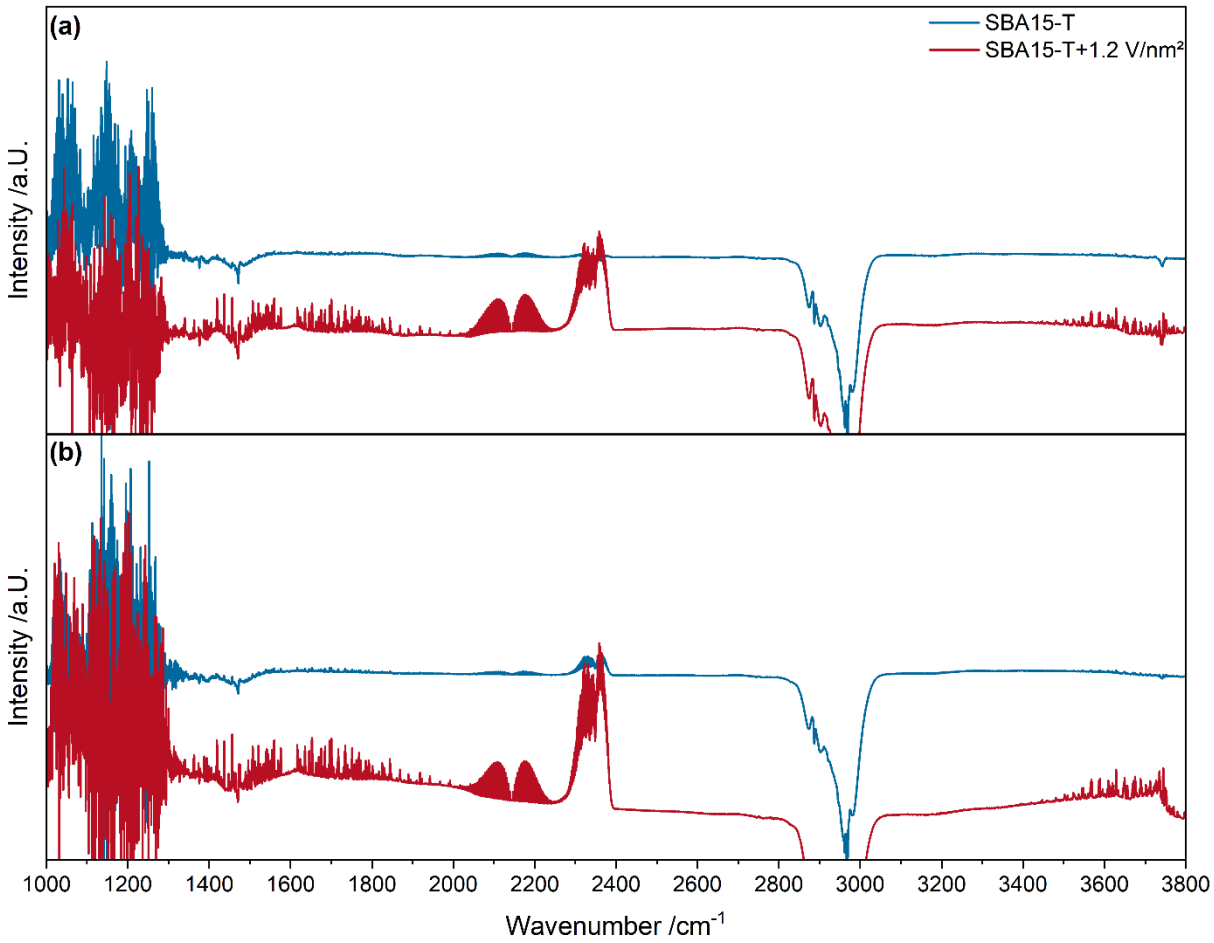

Figure S29: PSD spectra of ALD synthesized samples at a phase shift of 360° during **(a)** constant oxygen and pulsed propane flow and **(b)** constant propane and pulsed oxygen flow.

In comparison to the P25 samples, the static operando DRIFT spectra show no dynamics for the SBA-15 based samples and are therefore not discussed further. In contrast, the ME-DRIFT spectra show some dynamics. The vanadyl peak shows a large degree of noise, which might be caused by the lower conversion or the very broad Ti-OH vibration in this region, but a deflection is still observed. The carbonate region shows almost no adsorbates, only one distinct one at ~1610 cm^{-1}, indicative of propylene formation. The carbonate and formate adsorbates observed for P25-based samples are not observed, as they are relevant for CO_x formation. Since the SBA-15-based samples have a lower conversion and a much better selectivity towards propylene and the MES intensity depends on the conversion, the absence of the signal is in good agreement with the catalytic activities. In addition, the same transient Ti-OH species as for the P25 based samples is observed at ~3740 cm^{-1}. The amount of Ti-OH species is also in agreement with the conversion, as observed for the P25-based

samples and shows a similar trend, indicating that the ALD-synthesized titania, even though the phase composition is different, catalyzes the initial C-H bond breakage similarly to the bulk titania samples. Since the Ti-OH peak for SBA15-T and the C=C as well as the Ti-OH peak are the only adsorbates present, no time constants are determined since the time evolution of adsorbates is not relevant for these few peaks. In summary, the SBA-15-based samples have a different structure and phase composition than the P25-based bulk titania samples, coordinating vanadia differently, leading to more oligomerization and locally higher vanadia densities due to the titania islands. However, the observed structural dynamics for both vanadia and titania are very similar and demonstrate a broader applicability of our mechanistic findings than only for specifically P25.

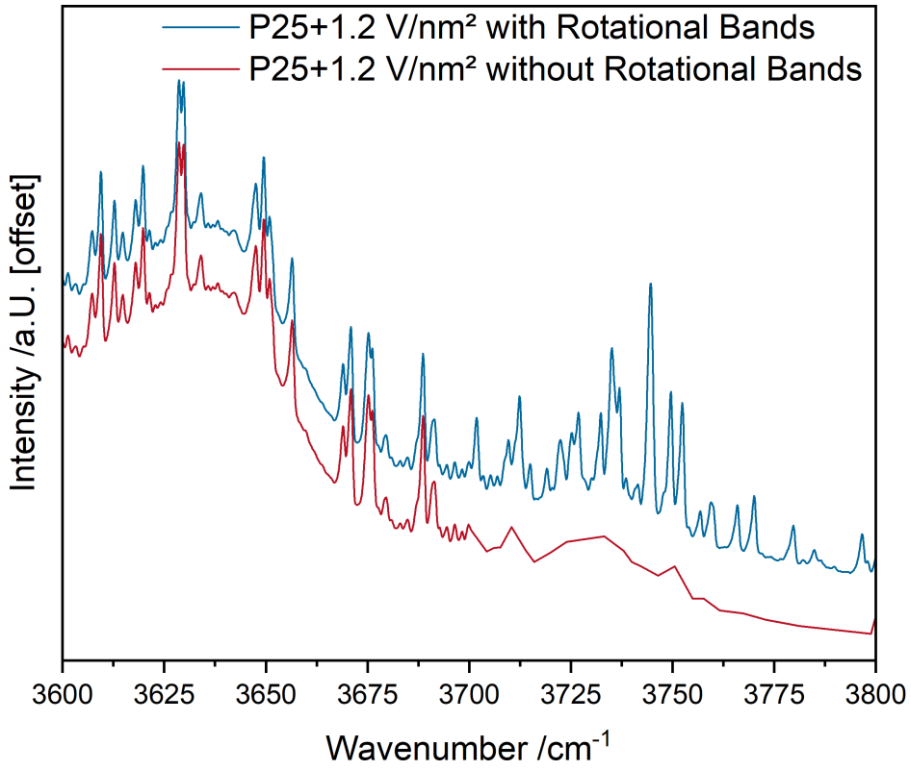

Figure S30: Exemplary removal of water rotational contributions from the Ti-OH region of the 360° PSD spectrum for the P25+1.2 V/nm sample to enable the quantification of the peak area within 3700-3780 cm^{-1}.

Table S5: Time constants determined from in-phase angle analysis of the PSD spectra of P25 and vanadia-loaded P25 samples. The experimental error for all values is the same value as for the P25+1.2 V/nm² samples (see Table 2).

P25		**P25+0.1 V/nm²**		**P25+0.5 V/nm²**		**P25+2.5 V/nm²**	
Wavenumber /cm^{-1}	Time /s	Wavenumber /cm^{-1}	Time /s	Wavenumber /cm^{-1}	Time /s	Wavenumber /cm^{-1}	Time /s
1618	33.3	1618	34.3	1613	33.3	3735	44.7
3741	34.3	1581	35.4	2028	34.3	1467	45.8
1562	37.4	2025	38.5	1990	35.4	1619	47.8
3611	37.4	3739	39.5	3739	35.4	3601	48.9
3673	39.5	3618	40.6	3602	37.4	1376	53
1438	46.8	3666	44.7	1475	38.5	1995	53
		1366	46.8	1368	39.5	2031	53
		1484	49.9	3641	40.6		

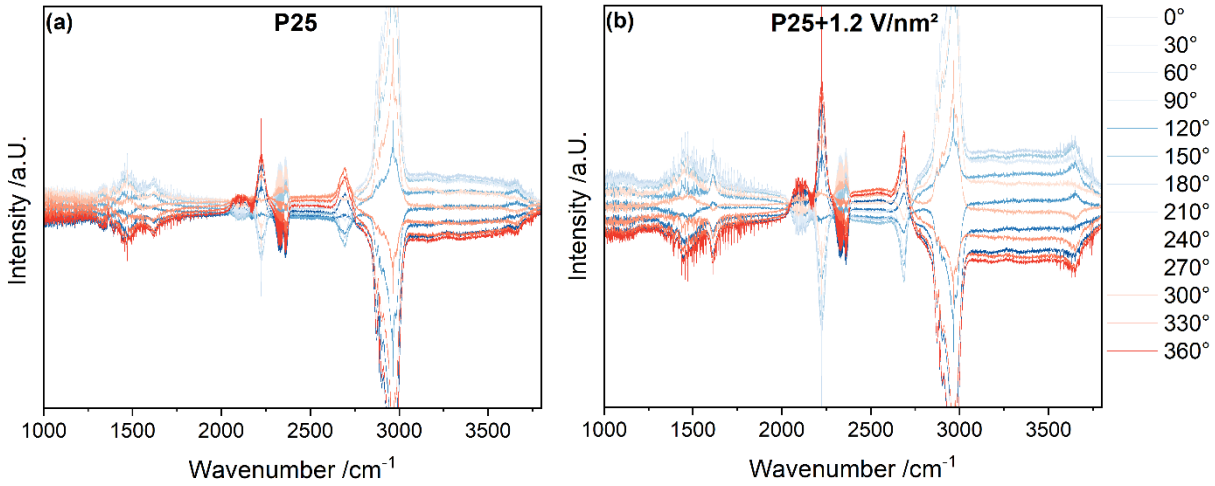

Figure S31: PSD spectra of **(a)** P25 and **(b)** P25+1.2 V/nm² between a 0° and 360° phase-shift in 30° steps during constant oxygen flow while the propane flow was constantly switched between C_3H_8 and C_3D_8.

References

(1) Nitsche, D.; Hess, C. Structure of Isolated Vanadia and Titania: A Deep UV Raman, UV–Vis, and IR Spectroscopic Study. *J. Phys. Chem. C* **2016**, *120* (2), 1025–1037. DOI: 10.1021/acs.jpcc.5b10317.

(2) Larrubia, M. A.; Busca, G. An ultraviolet–visible–near infrared study of the electronic structure of oxide-supported vanadia–tungsta and vanadia–molybdena. *Mater. Chem. Phys.* **2001**, *72* (3), 337–346. DOI: 10.1016/s0254-0584(01)00329-7.

(3) Landmann, M.; Rauls, E.; Schmidt, W. G. The electronic structure and optical response of rutile, anatase and brookite TiO_2. *J. Condens. Matter Phys.* **2012**, *24* (19), 195503. DOI: 10.1088/0953-8984/24/19/195503.

(4) Tian, G.-L.; He, H.-B.; Shao, J.-D. Effect of Microstructure of TiO_2 Thin Films on Optical Band Gap Energy. *Chin. Phys. Lett.* **2005**, *22* (7), 1787–1789. DOI: 10.1088/0256-307X/22/7/062.

(5) Lian, Z.; Deng, H.; Xin, S.; Shan, W.; Wang, Q.; Xu, J.; He, H. Significant promotion effect of the rutile phase on V_2O_5/TiO_2 catalysts for NH_3-SCR. *Chem. Commun.* **2021**, *57* (3), 355–358. DOI: 10.1039/d0cc05938b.

(6) Sobel, N.; Hess, C. Nano-laminating of SiO_2 and TiO_2 : Atomic layer deposition as a tool to gain new insight into interfaces. *MRS Proc.* **2015**, *1805.* DOI: 10.1557/opl.2015.554.

(7) Samek, I. A.; Bobbitt, N. S.; Snurr, R. Q.; Stair, P. C. Interactions of VO_x Species with Amorphous TiO_2 Domains on ALD-Derived Alumina-Supported Materials. *J. Phys. Chem. C* **2019**, *123* (13), 7988–7999. DOI: 10.1021/acs.jpcc.8b07424.

(8) Scheurell, K.; Hoppe, E.; Brzezinka, K.-W.; Kemnitz, E. Bulk and surface properties of highly dispersed VO_x/ZrO_2, VO_x/SiO_2 and $VO_x/TiO_2/SiO_2$ systems and their relevance for propane oxidation. *J. Mater. Chem.* **2004**, *14* (16), 2560. DOI: 10.1039/b402924k.

(9) Kaichev, V. V.; Popova, G. Y.; Chesalov, Y. A.; Saraev, A. A.; Andrushkevich, T. V.; Bukhtiyarov, V. I. Active component of supported vanadium catalysts in the selective oxidation of methanol. *Kinet. Catal.* **2016**, *57* (1), 82–94. DOI: 10.1134/S0023158416010043.

(10) Nawaz, R.; Kait, C. F.; Chia, H. Y.; Isa, M. H.; Huei, L. W. Glycerol-Mediated Facile Synthesis of Colored Titania Nanoparticles for Visible Light Photodegradation of Phenolic Compounds. *Nanomaterials* **2019**, *9* (11). DOI: 10.3390/nano9111586. Published Online: Nov. 8, 2019.

(11) Göpel, W.; Anderson, J.A.; Frankel, D.; Jaehnig, M.; Phillips, K.; Schäfer, J.A.; Rocker, G. Surface defects of TiO_2(110): A combined XPS, XAES and ELS study. *Surf. Sci.* **1984**, *139* (2-3), 333–346. DOI: 10.1016/0039-6028(84)90054-2.

(12) Gross, T.; Ramm, M.; Sonntag, H.; Unger, W.; Weijers, H. M.; Adem, E. H. An XPS analysis of different SiO_2 modifications employing a C 1s as well as an Au $4f_{7/2}$ static charge reference. *Surf. Interface Anal.* **1992**, *18* (1), 59–64. DOI: 10.1002/sia.740180110.

(13) Spende, A.; Sobel, N.; Lukas, M.; Zierold, R.; Riedl, J. C.; Gura, L.; Schubert, I.; Moreno, J. M. M.; Nielsch, K.; Stühn, B.; Hess, C.; Trautmann, C.; Toimil-Molares, M. E. TiO_2, SiO_2, and Al_2O_3 coated nanopores and nanotubes produced by ALD in etched ion-track membranes for transport measurements. *Nanotechnology* **2015**, *26* (33), 335301. DOI: 10.1088/0957-4484/26/33/335301. Published Online: Jul. 30, 2015.

(14) Burcham, L. J. In situ IR, Raman, UV-Vis DRS spectroscopy of supported vanadium oxide catalysts during methanol oxidation. *Top. Catal.* **2000**, *11/12* (1/4), 85–100. DOI: 10.1023/A:1027275225668.

(15) Won, J. M.; Kim, M. S.; Hong, S. C. Effect of vanadium surface density and structure in VO_x/TiO_2 on selective catalytic reduction by NH_3. *Korean J. Chem. Eng.* **2018**, *35* (12), 2365–2378. DOI: 10.1007/s11814-018-0158-x.

(16) Jaegers, N. R.; Lai, J.-K.; He, Y.; Walter, E.; Dixon, D. A.; Vasiliu, M.; Chen, Y.; Wang, C.; Hu, M. Y.; Mueller, K. T.; Wachs, I. E.; Wang, Y.; Hu, J. Z. Mechanism by which Tungsten Oxide Promotes the Activity of Supported V_2O_5/TiO_2 Catalysts for NO_x Abatement: Structural Effects Revealed by ^{51}V MAS NMR Spectroscopy. *Angew. Chem. Int. Ed.* **2019**, *58* (36), 12609–12616. DOI: 10.1002/anie.201904503.

(17) Schumacher, L.; Hess, C. The active role of the support in propane ODH over VO_x/CeO_2 catalysts studied using multiple operando spectroscopies. *J. Catal.* **2021**, *398* (13), 29–43. DOI: 10.1016/j.jcat.2021.04.006.